pubs.acs.org/NanoLett Letter

Deep Learning Enabled Strain Mapping of Single-Atom Defects in Two-Dimensional Transition Metal Dichalcogenides with Sub-Picometer Precision

Chia-Hao Lee, Abid Khan,[#] Di Luo,[#] Tatiane P. Santos, Chuqiao Shi, Blanka E. Janicek, Sangmin Kang, Wenjuan Zhu, Nahil A. Sobh, André Schleife, Bryan K. Clark, and Pinshane Y. Huang*

Cite This: *Nano Lett.* 2020, 20, 3369−3377 Read Online

ACCESS | Metrics & More | Article Recommendations | Supporting Information

ABSTRACT: Two-dimensional (2D) materials offer an ideal platform to study the strain fields induced by individual atomic defects, yet challenges associated with radiation damage have so far limited electron microscopy methods to probe these atomic-scale strain fields. Here, we demonstrate an approach to probe single-atom defects with sub-picometer precision in a monolayer 2D transition metal dichalcogenide, $WSe_{2-2x}Te_{2x}$. We utilize deep learning to mine large data sets of aberration-corrected scanning transmission electron microscopy images to locate and classify point defects. By combining hundreds of images of nominally identical defects, we generate high signal-to-noise class averages which allow us to measure 2D atomic spacings with up to 0.2 pm precision. Our methods reveal that Se vacancies introduce complex, oscillating strain fields in the $WSe_{2-2x}Te_{2x}$ lattice that correspond to alternating rings of lattice expansion and contraction. These results indicate the potential impact of computer vision for the development of high-precision electron microscopy methods for beam-sensitive materials.

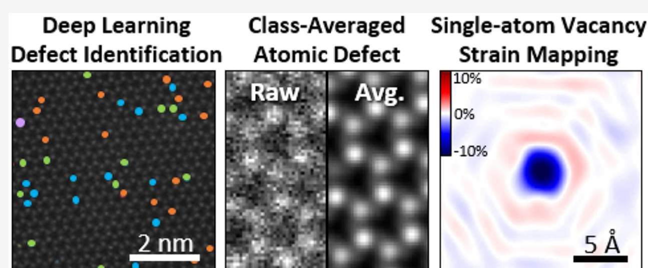

KEYWORDS: *Deep learning, fully convolutional network, single-atom defects, strain mapping, scanning transmission electron microscopy, 2D materials*

Downloaded via UNIV ILLINOIS URBANA-CHAMPAIGN on May 24, 2020 at 04:33:07 (UTC).
See https://pubs.acs.org/sharingguidelines for options on how to legitimately share published articles.

A key challenge in characterizing two-dimensional (2D) materials is determining the structure of defects with sub-picometer precision. Defect and strain engineering of 2D materials are emerging tools to tune the optical and electronic properties of atomically thin layers.[1−3] Yet, while techniques such as aberration-corrected scanning transmission electron microscopy (STEM) have the spatial resolution to image each atom in 2D materials, the precision of atom-by-atom electron microscopy has so far been limited to the scale of 8−20 pm, or strains on the order of 3% or more.[4−6] While these methods can detect the relatively large strains at the nearest-neighbor sites of vacancies, the corresponding local strains (≈1%) expected to result from substitutions and long-range strain fields from point defects have so far been below the detection limits of atomic-resolution (S)TEM.

This precision is fundamentally limited by signal-to-noise ratio (SNR).[7] High radiation doses are required to precisely measure the position of single atoms, yet ionization and knock-on damage alter the structure of defects at high electron dose for 2D materials,[8−10] severely limiting the achievable SNR. In bulk materials where the precision is limited by microscope instabilities rather than electron beam damage, the measurement precision can be enhanced by acquiring a series of images on the same region, then combining the resulting data to minimize image distortion or achieve higher SNR using techniques such as drift correction (10 pm),[11] template matching (5−15 pm),[12,13] rigid (5 pm),[14] and nonrigid registration (0.3−0.9 pm).[15] Note that precision better than spatial resolution in (S)TEM imaging is routinely achieved[5,6,11−15] since they represent two different aspects of a measurement: Precision is the statistical spread of measured distances in an image, while resolution is the smallest distance between two objects that remains distinguishable for an imaging system. On their own, these approaches have limited utility for measuring the intrinsic structure of 2D materials because they typically require high doses on the order of 10^8−10^9 e^-/nm^2, above the damage thresholds for many 2D materials. For example, serious electron beam damage of free-standing, monolayer MoS_2 has been observed after an electron dose of 2.8×10^8 e^-/nm^2 at 80 kV[9]. Meanwhile, diffraction-based strain measurements such as nanobeam electron diffraction[16] can measure sub-picometer (sub-pm) strains in

Received: January 20, 2020
Revised: April 2, 2020
Published: April 3, 2020

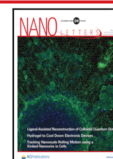

© 2020 American Chemical Society

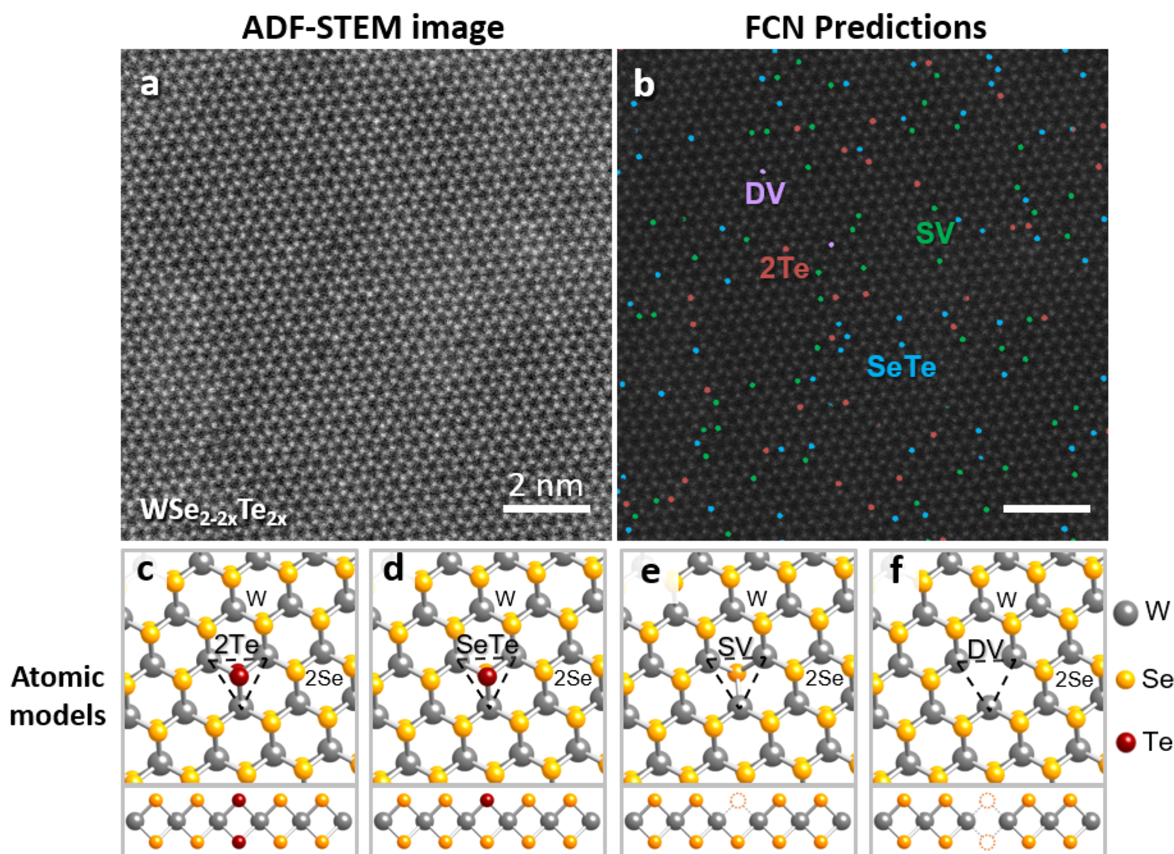

Figure 1. Deep learning-enabled identification and classification of point defects in ADF-STEM image. (a) Atomic-resolution ADF-STEM image of $WSe_{2-2x}Te_{2x}$. To minimize image distortions, the data are acquired as 10 sequential frames with short dwell times and then frame-averaged. The total dose is 1.24×10^7 e^-/nm^2. (b) Chalcogen-site defects identified by FCNs overlaid on image from (a). Labels indicate one or two Te substitutions (SeTe and 2Te, respectively) and single or double Se vacancies (SV and DV). (c−f) Top- and side-view schematics of defect structures. The chalcogen defect centers are marked with dashed triangles.

2D transition metal dichalcogenides (TMDCs), but are limited to a spatial resolution of a few nanometers. These challenges mean that for 2D materials, existing techniques exhibit a trade-off between spatial resolution and the precision with which strain can be measured, making it difficult to measure the strain field of atomic defects. Yet at the same time, 2D materials offer a profound opportunity for understanding atomic-scale strain. Because they are only a single unit cell thick, 2D materials are ideal for demonstrating high precision characterization methods, such as the ability to characterize how each atom in a material responds to local perturbations.[4,6,17−19]

Here, we apply machine learning to locate and classify each point defect in large data sets of atomic-resolution images, then use the resulting data to generate class-averaged images of single-atom defects in 2D materials. This method enables sub-pm precision measurements of beam-sensitive structures because it combines information measured from large numbers of nominally identical defects while limiting the dose to any individual atom. Our approach is analogous to the class-averaging methods used in single particle cryo-electron microscopy, where they are used to aid in solving the structure of biological macromolecules and viruses.[20]

We demonstrate our approach using an alloyed 2D TMDC, monolayer $WSe_{2-2x}Te_{2x}$. Previously, STEM has been used to directly measure the local variations in the concentration, ordering, and properties of alloyed TMDCs.[21−24] We synthesized 2H-$WSe_{2-2x}Te_{2x}$ using cooling-mediated, one-step chemical vapor deposition (CVD) on SiO_2/Si substrates. The $WSe_{2-2x}Te_{2x}$ was then transferred to TEM grids using a wet-transfer technique (see Supporting Information (SI)). These methods produce suspended flakes of predominately monolayer $WSe_{2-2x}Te_{2x}$ that are 10−20 μm across. These $WSe_{2-2x}Te_{2x}$ samples naturally contain point defects including Te substitutions and Se vacancies which provide local lattice distortions that can be used to test our techniques.

We next acquired aberration-corrected annular dark-field (ADF) STEM images (Figure 1a) and used machine learning to locate and classify the defects present, as illustrated in Figure 1. Each "single" STEM image was acquired as 10 sequential frames with short dwell times (2 μs/pixel) in the same region and then frame-averaged. Similar methods have been previously shown to minimize image distortions from sample drift to enable high-precision strain measurements from STEM images.[14,15,25] The image distortions that result from long acquisition times are shown in Figure S9. The accumulated dose for these frame-averaged images is 1.24×10^7 e^-/nm^2 with an equivalent dwell time of 20 μs/pixel. This dose lies in the typical range for 2D TMDCs imaging and is below the dose threshold to cause significant damage to the lattice. As shown in Figure S1, these frame-averaged images are comparable or even better in SNR than single-frame images acquired with the same dose. For this study, we analyzed images of 9 different regions, spanning a total area of 4000 nm^2, or approximately 130,000 atoms. To analyze the data, we trained a deep learning model based on fully convolutional networks (FCNs) with ResUNet architecture to locate and

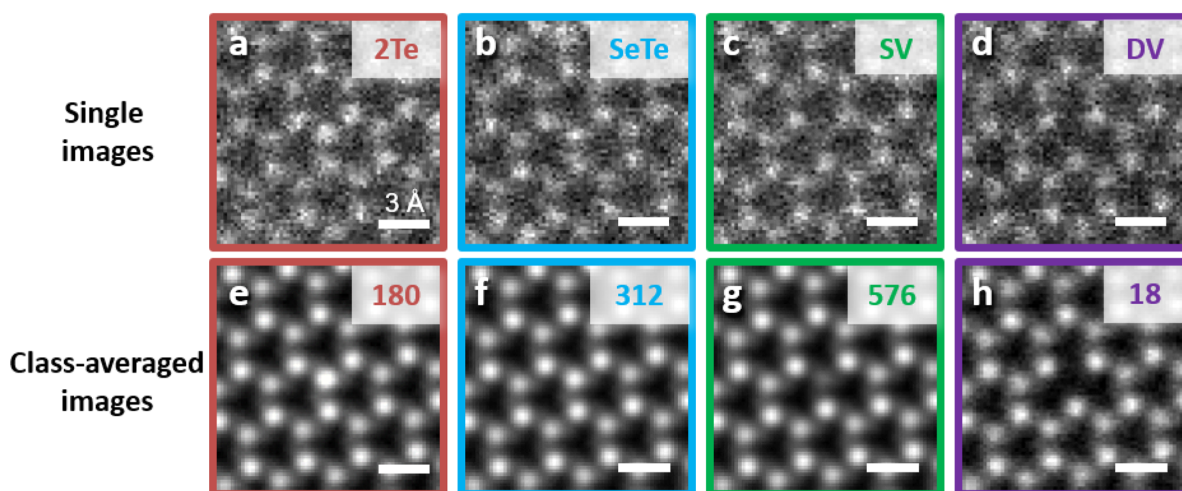

Figure 2. Comparisons between single and class-averaged images of 2Te, SeTe, SV, and DV defects. (a−d) Representative single images of FCN-identified defects sectioned from Figure 1a. We did not apply any smoothing, Fourier filtering, or probe deconvolution to our STEM images. By aligning and summing many equivalent lattice sites using rigid-registration, we produce high SNR, class-averaged images (e−h) from nominally identical point defects. The number of images summed is labeled at the top right corner of each image.

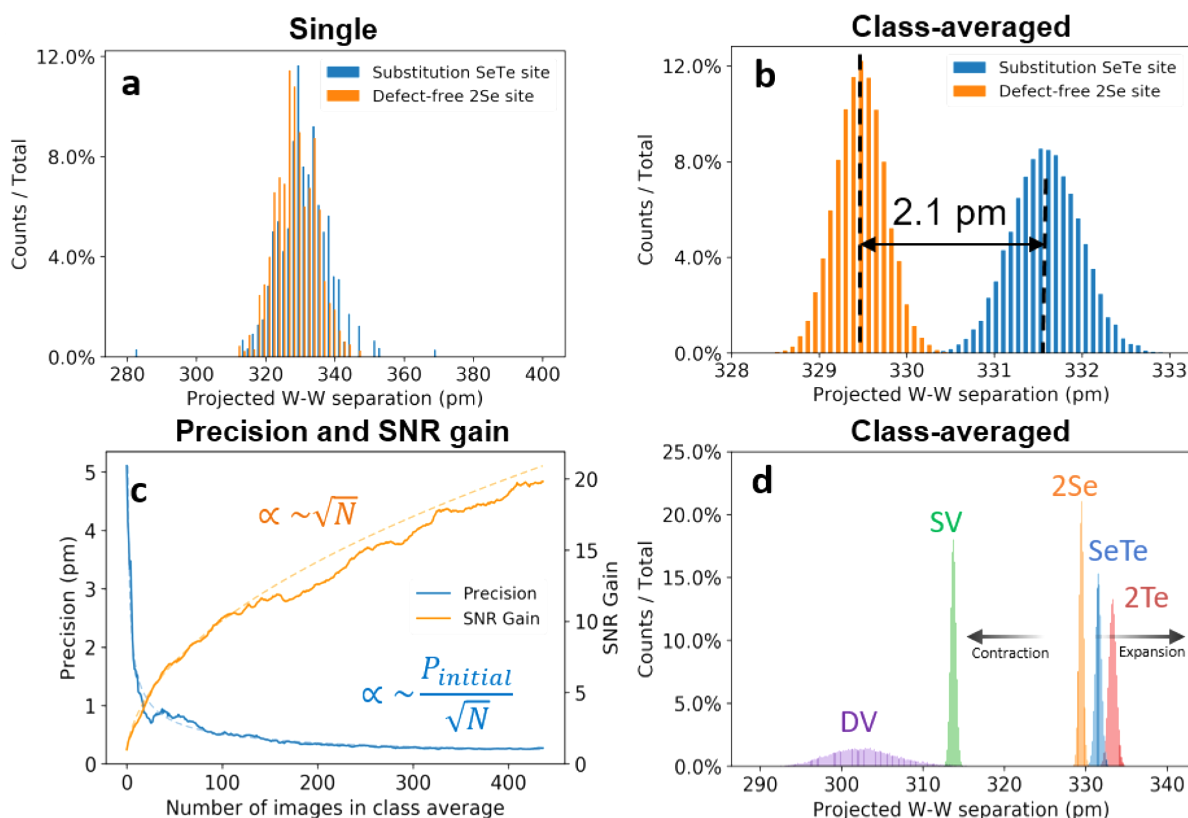

Figure 3. Impact of class averaging on signal-to-noise and precision of atomic separations. (a,b) Distributions of projected W−W separations nearest to the defect site in (a) individual (b) class-averaged images generated by summing 312 single Te substitution (SeTe) and 437 defect-free (2Se) images, respectively. Class-averaged distributions are generated through bootstrapping. Unlike in the individual images, the class-averaged images show well-separated distributions of W−W separation measurements of SeTe substituted and defect-free 2Se sites. From class averaging, the measured W−W separation is 331.6 ± 0.4 pm at SeTe substituted sites and 329.5 ± 0.3 pm at defect-free 2Se sites. (c) Precision and SNR gain as a function of summed images N. The precision scales with $P_{\text{initial}}/\sqrt{N}$, while the SNR gain scales with $\sqrt{N}$ due to the reduction of Poisson noise. (d) Distributions of projected W−W separations measured on class-averaged images of defect-free 2Se sites and each defect types (2Te, SeTe, SV, DV), which yielded local strains of 1.2 ± 0.2%, 0.6 ± 0.2%, −4.8 ± 0.1%, and −8 ± 1%, respectively.

classify the point defects in $WSe_{2-2x}Te_{2x}$, producing 2D maps of the defect positions (Figure 1b). Neural networks have already revolutionized image recognition in fields such as medical diagnosis, weather forecasting, and facial recognition; recently, they have also been applied to identify atomic defects in atomic-resolution (S)TEM images.[26−28] Conventionally, defect detection has been a labor-intensive task which is often done by hand[6,22] or simple image processing such as Fourier

https://dx.doi.org/10.1021/acs.nanolett.0c00269
Nano Lett. 2020, 20, 3369−3377

filtering[29] or intensity thresholding.[24,30] Neural networks offer an opportunity to automate defect identification, making it possible to efficiently locate large numbers of defects to generate class averages systematically while minimizing human intervention. We trained FCNs using simulated data generated via incoherent image simulations using Computem.[31,32] In order to make our simulations more realistic, we apply a set of postprocessing steps to the images, including the addition of Gaussian noise, probe jittering, image shear, and varying spatial sampling, to create our final training data. Similar methods are well-established in the literature,[26−28] though we found that we achieved the highest classification precision on experimental data by introducing low-frequency contrast variations in the simulated data to emulate surface contamination. We found that these methods yielded a true positive rate of 98%. When we compared the true positive rate with FCNs trained directly on hand-labeled experimental data, we found that the simulation-trained data performed comparably to FCNs trained on experimental data but with considerably less manual labor (see SI for evaluation metrics). The source codes for training set generation and model training are freely available on Github at: github.com/ClarkResearchGroup/stem-learning/.

We focused on the four primary types of chalcogen-site defects present in our samples, which we refer to as 2Te, SeTe, SV, and DV (see Figure 1c−f). Our naming convention describes the composition and filling of the chalcogen sites in $WSe_{2-2x}Te_{2x}$. In projection, the chalcogen columns can contain either two Se atoms (no defects, 2Se), one or two Te substitutions (SeTe and 2Te, respectively), or one or two Se vacancies (SV and DV). These defects are the most common point defects we observed in $WSe_{2-2x}Te_{2x}$. Using the large data sets probed by FCN, we conducted population analyses of the defects present in $WSe_{2-2x}Te_{2x}$. We calculated both the total number and concentrations (over all 86,000 chalcogen sites) of each defect type in our experimental images. We found the Te fraction in our samples is $WSe_{2-2x}Te_{2x}$ where $x = 0.06$. Meanwhile, 3% of chalcogen sites are occupied by vacancies; this number is an upper bound of the as-grown vacancy concentration because TEM sample fabrication and electron irradiation can induce additional vacancies. We found that metal-site defects were extremely rare (comprising less than 0.04% of metal sites), and we did not observe columns containing a single Te atom (1Te).

Next, we generated class-averaged images of each defect type from the FCN outputs (Figure 2). From the thousands of defects identified via the FCN, we selected only isolated defects, that is, defects that were separated by a distance $d \geq 6.6$ Å (roughly 4 × 4 unit cells) from any other defects. This step dramatically reduced the number of defects used for class averaging, but it allowed us to study the structure of the defects with minimal external perturbations. The use of FCNs enabled this extra selection process because it allowed us to locate a sufficiently large population to retain several hundred defects in each class after this step. We then sectioned the original images into small windows centered around each individual defect as shown in Figure 2a−d. In order to avoid the introduction of image artifacts, we did not apply any smoothing, Fourier filtering, or probe deconvolution to our STEM images. The sectioned images were grouped by defect type, creating image stacks containing 180 2Te, 312 SeTe, 576 SV, 18 DV individual defects and 437 defect-free 2Se regions. Finally, we aligned and summed each image stack using rigid registration,[25] producing the high SNR class-averaged images shown in Figure 2e−h.

As shown in Figure 3, class averaging enables sub-pm precision measurements of atomic spacings and local strains. In Figure 3a, we used 2D Gaussian fitting to determine the positions of atomic columns in a series of single images, measure the three nearest W−W spacings around SeTe substitutions, and compare them with the same measurements in defect-free images. We obtained W−W spacings of 330 ± 8 pm (std. dev.) for the SeTe substitution and 330 ± 6 pm for defect-free 2Se sites. The histograms in Figure 3a overlap heavily, indicating that single images cannot be used to distinguish the local strains around a single Te substitution. The 6−8 pm precision we obtained for single images is comparable to or better than similar measurements previously reported for 2D materials,[4−6] indicating the high quality of our starting data.

In contrast, Figure 3b shows the well-separated distributions of W−W spacings measured from class-averaged images. To generate these distributions, we apply a bootstrap approach commonly used in statistical analysis[33] to produce several class-averaged images using randomly selected subsets of images from the original image stack. These bootstrapped class averages allow us to estimate the measurement precision using the same definition as for single images (see Figure S5). For the class-averaged data, we measure W−W separations of 331.6 ± 0.4 pm around the Te substitution (summing 312 images for each class average) and 329.5 ± 0.3 pm for the defect-free site (using 437 images). Additionally, we evaluated the accuracy of the measurement by calculating the average deviation between W−W separations along 3 equivalent lattice directions. We obtained an average deviation of 0.2 pm, a value that is consistent with the image distortion predicted by the sample drift rate (5 pm/sec). This indicates our 0.3 pm precision approaches the accuracy limit (0.2 pm) set by instrumental drift. These data show the utility of class averaging, which provided a 20-fold improvement in precision when summing 437 images, sufficient to measure local strains on the order of 0.1%. Notably, the sub-pm precision obtained using our class-averaging approach is comparable to the highest precision electron microscopy measurements obtained via multiframe averaging in bulk materials,[15] but without increasing the dose per unit area. Importantly, the dose needed to acquire a single image of one Se vacancy with equivalent SNR is 7.14×10^9 e^-/nm^2, a dose that causes severe damage to monolayer $WSe_{2-2x}Te_{2x}$ (see Movie S1). This approach allows us to access the small strains around atomic defects in 2D materials while minimizing electron beam damage.

The sub-pm precision obtained in the class-averaged images is a direct result of their increased SNR. Figure 3c plots the precision and SNR gain in class-averaged images as a function of the number of images summed, ranging from 1 to 437 defect-free regions. In order to generate this plot, we quantified the statistical spread of measured distances between equivalent atomic columns in a defect-free lattice, similar to the approach used in ref 15 that does not involve bootstrapping (see Figure S6). The gain in the SNR, which is defined as SNR_{sum}/SNR_{raw}, scales as $\sqrt{N}$, where N is the number of images summed. Meanwhile, the measurement precision of the atomic spacings scales as $P_{initial}/\sqrt{N}$ and eventually approaches 0.3 pm, in excellent agreement with the value obtained using bootstrapping. These scaling laws arise because Poisson noise is the

https://dx.doi.org/10.1021/acs.nanolett.0c00269
Nano Lett. 2020, 20, 3369−3377

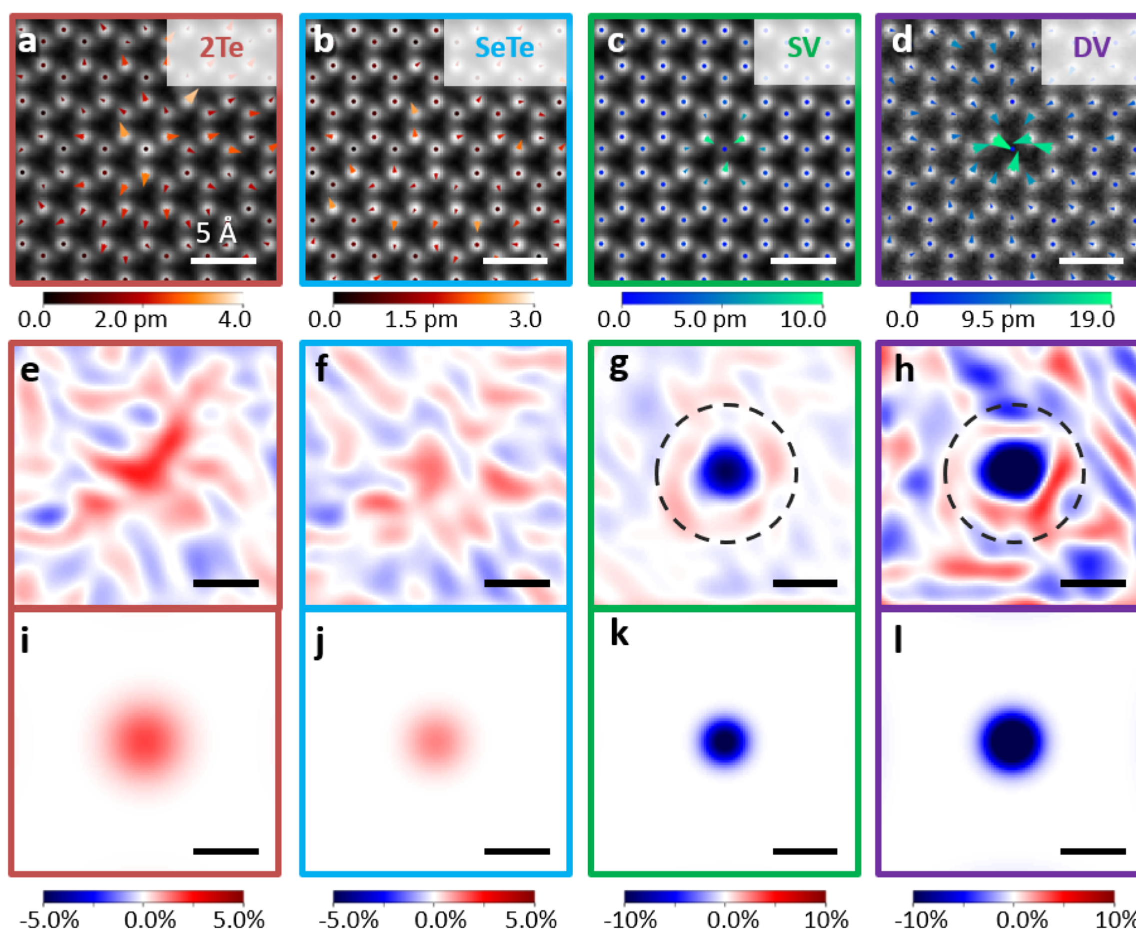

Figure 4. Displacement and strain fields for chalcogen site defects. (a−d) Two-dimensional displacement vector field overlaid on class-averaged images of chalcogen site defects. The vectors are enlarged for visibility by 40 times in (a,b) and 10 times in (c,d). (e−h) Experimental dilation fields calculated from the displacement fields. The dilation corresponds to the local projected area change. (e) 2Te and (f) SeTe exhibit local expansion, while (g) SV and (h) DV exhibit local contraction. (i−l) Best-fit dilation fields calculated with 2D isotropic elastic continuum theory using Eshelby's inclusion model.

dominant source of noise in the ADF-STEM detector.[7,25] Figure 3d shows the distributions of nearest-neighbor W−W atomic spacings for each class-averaged defect type measured via bootstrapping. The variation in the widths of these distributions, such as the wide distribution of DV, mainly results from differences in the number of defects summed. The distributions for each defect type are well separated, indicating that we are able to distinguish the local lattice expansion from single and double Te substitutions as well as the contraction that results from single and double Se vacancies after class averaging.

Next, we measured the displacement and strain fields for each defect type. Figure 4a−d shows magnified 2D displacement vectors overlaid on class-averaged defect images. Displacement vectors are obtained by comparing the positions of each atomic column on class-averaged defect images to the positions measured in a defect-free, class-averaged reference image. Single (SV) and divacancies (DV) correspond with a local contraction of the lattice, while single (SeTe) and double (2Te) substitutions produce a local expansion. The magnitude of the displacement vectors decays quickly as a function of distance from the defect centers, for example, dropping below 1 pm within 3 unit cells for a single Te substitution. To better visualize the local distortions, we calculated the 2D strain tensor components (ϵ_{xx}, ϵ_{xy}, ϵ_{yx}, and ϵ_{yy}) for each defect type. Density functional theory (DFT) simulations indicate that these in-plane strain components are much larger than out-of-plane deformation and that as a result, the 2D strain fields measured from the 2D projections in STEM images are a good approximation of the full 3D deformation. The continuous strain maps are generated by first interpolating the discrete 2D displacement vectors and then taking spatial derivatives along the x and y directions (see Figure S7 for more details). While the strain tensor is only formally defined at positions halfway between each pair of atomic sites, the interpolated strain fields are commonly utilized because there is a standardized method to compute them and because they well-suited for comparisons to continuum models. For comparison, we also computed the discrete version of the 2D strain components, which reproduces all the main features of the continuous version (see Figure S8).

Figure 4e−h shows the experimental dilation maps, which correspond to local 2D area change associated with each defect, calculated as the sum of the diagonal components ϵ_{xx} + ϵ_{yy} of the strain tensor. We compared these experimental dilation fields to those calculated using a purely elastic continuum theory. To calculate the strain field that would result from an ideal elastic medium, we use the 2D version of Eshelby's inclusion model, where the crystal is modeled as an infinite, isotropic 2D elastic continuum under deformation

https://dx.doi.org/10.1021/acs.nanolett.0c00269
Nano Lett. 2020, 20, 3369−3377

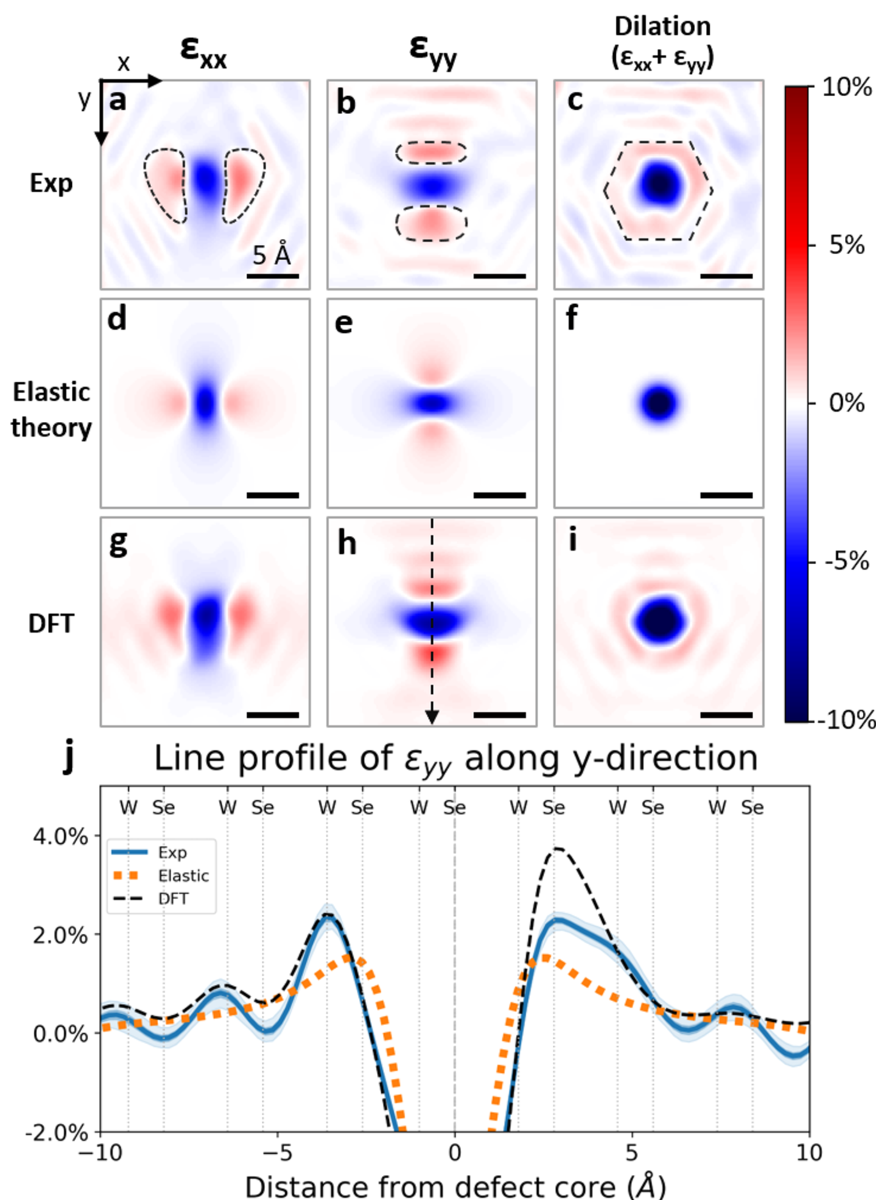

Figure 5. Strain fields at single Se vacancy. (a−c) Experimental strain fields calculated from the derivative of displacement field. Compared to Figure 4g, Figure 5 utilizes a larger data set of 2939 single Se vacancies. (d−f) Best-fit strain fields calculated by elastic theory using Eshelby's inclusion model. (g−i) Strain fields calculated from DFT simulations of defect relaxation. The anisotropic features show a good match with the experimental data (a,b). (j) Line profiles of experimental, elastic theory, and DFT-derived ϵ_{yy} across the vacancy, as marked by dashed arrow. The shaded regions of the experimental line profile correspond to the full-range of the experimental distribution of strain values (±0.25%), while the standard deviation is measured to be 0.1% using bootstrapping. In contrast to the monotonically decaying strain field predicted by continuum elastic theory, both experimental and DFT profiles show oscillations in the strain field. Vertical lines indicate the locations of W and Se columns.

from a point-like inclusion.[34−36] While the best-fit elastic models (Figure 4i−l) capture the behavior of the experimental dilation fields near the defect core (Figure 4e−h), we also notice key differences, discussed below. While they are not surprising, deviations from the continuum elastic models have remained challenging to observe; indeed in many cases, continuum models have remained a good fit to strain fields in 2D materials to within the measurement precision.[4,36]

Figure 5 compares the ϵ_{xx}, ϵ_{yy}, and dilation components of experimental strain fields from a single vacancy (Figure 5a−c) to both a best-fit elastic continuum theory (Figure 5d−f), and first-principles simulations using DFT (Figure 5g−i). To more precisely compare the differences between experimental data and models, we used the methods described above to acquire and process a larger experimental data set of 2939 single vacancies. This produced a precision of 0.2 pm, a regime where the measurement error is limited by sample drift and instrument instabilities rather than signal-to-noise. Compared with the equivalent data in Figure 4g, the higher precision in Figure 5c makes apparent 6-fold symmetric periodic oscillations in the dilation field, centered around the vacancy. Although the exact appearance of the strain field oscillations does depend on the interpolation process, they are apparent in the displacement vectors before interpolation, which oscillate in strength along the radial direction.

In order to calculate strain fields from DFT simulations, we conducted structural relaxations of both the SV and defect-free lattice (see SI). A 9 × 9 supercell was required to avoid

https://dx.doi.org/10.1021/acs.nanolett.0c00269
Nano Lett. 2020, 20, 3369−3377

coupling of the strain field between defects when using periodic boundary conditions. Using the relaxed atomic coordinates, we simulated ADF-STEM images using a multislice algorithm implemented in Computem[31] and then applied the same methods used for our experimental data to calculate the DFT-derived strain fields.

The experimental strain fields deviate from continuum elastic theory in two main ways. First, they are not isotropic in 2D but instead reflect the symmetry of the lattice. For example, the regions marked by the black dashed lines in Figure 5a have higher intensity in the top half of the image. Similarly, the experimental ϵ_{yy} is asymmetric across the center of the defect (Figure 5b). These asymmetries are present in the DFT simulations (Figure 5g,h), but not in the continuum elastic model, which predicts 2-fold symmetric ϵ_{xx} and ϵ_{yy} (Figure 5d,e) due to its isotropic nature. Second, while the dilation field calculated using the continuum elastic model indicates only local contraction around the vacancy (Figure 5f), we observe alternating rings of contraction and expansion in the DFT data (Figure 5i) and in experiment (Figure 5c), forming a radially oscillating strain field. Radial strain field oscillations were first predicted in the mid-1950s[37,38] around point defects in face-centered cubic crystals. By enabling high-precision measurements of strain at atomic resolution in 2D materials, our methods now allow these strain field oscillations to be directly observed.

We investigate these strain field oscillations in more detail in the line profile of ϵ_{yy} in Figure 5j. In this plot, the mean experimental strain profile is shown in dark blue, while blue shading indicates the range of strain values calculated via bootstrapping. In the continuum elastic model (orange), the strain field monotonically decays away from the defect core, whereas the DFT (black) and experiment (blue) show clear oscillations up to a nanometer away from the defect core. Overall, we find excellent agreement between experiment and DFT-PBE, particularly for the locations of maxima and minima of strain field oscillations. The observation of these strain field oscillations is made possible because our approach achieves a sub-pm measurement precision previously only obtained by nanobeam diffraction in 2D materials,[16] but now at atomic resolution. We do note that the peak experimental strain field is smaller in magnitude than in the DFT. This likely occurs because DFT-PBE is known to underestimate elastic constants relative to experiment with a generalized-gradient approximation for exchange and correlation.[39] Passivation of some vacancies is another possible contributing factor.

To understand the origin and significance of these strain field oscillations, we note that similar phenomena have been predicted in both bulk metals[40] and ceramics.[41] In metals, radially oscillating strain fields may arise from defect-induced charge redistribution such as Friedel oscillations,[42] while for ionic crystals, Coulomb interactions between charge perturbations at defect site and ion cores of opposite signs lead directly to oscillations in the strain field. Either of these effects may contribute to the features we see in $WSe_{2-2x}Te_{2x}$. Accurate models for these complex strain fields were part of the historical motivation for the development of lattice static methods such as the Kanzaki method[37] and Green's function methods for modeling point defects in crystals.[43,44] In this context, direct observation of radially oscillating strain fields in 2D materials indicates both a new milestone in the ability to test and refine high-accuracy mechanical models for defects in crystals and a need to account for long-range strain fields when modeling defects in atomically thin materials.

In conclusion, we have developed techniques based on machine learning and aberration-corrected STEM to visualize the strain fields induced by single-atom defects in 2D materials. We used these methods to directly observe the strain fields of vacancies and substitutions in $WSe_{2-2x}Te_{2x}$, where the sub-pm precision enabled by class averaging revealed oscillations in the strain field around chalcogen vacancies that deviate from isotropic elastic continuum theory but agree well with DFT simulations. We show that deep learning enables the first direct imaging of radial strain field oscillations around vacancies, a phenomenon originally predicted in the mid-1950s[37,38] but never experimentally imaged. A key advantage of these methods is that they enable high precision measurements of beam-sensitive materials by leveraging computer vision to mine atomic-resolution data sets without requiring any changes in instrumentation. These methods should be particularly useful for studying 2D materials and other radiation-sensitive crystals and elucidating the complex strain phenomena that arise from structural rearrangements and defect−defect interactions. Going forward, our deep learning enabled class averaging can be applied in principle to any atomic resolution electron microscopy data sets, including spectrum imaging and four-dimensional STEM.

■ ASSOCIATED CONTENT

Supporting Information

The Supporting Information is available free of charge at https://pubs.acs.org/doi/10.1021/acs.nanolett.0c00269.

$WSe_{2-2x}Te_{2x}$ synthesis, TEM sample fabrication, ADF-STEM acquisition parameters, FCN model architecture and training setup, FCN model performance evaluation, bootstrapping process and strain analysis, and details of DFT calculation (PDF)

Movie S1: A series of sequential STEM images of $WSe_{2-2x}Te_{2x}$ showing the impact of electron dose on the atomic structure (AVI)

■ AUTHOR INFORMATION

Corresponding Author

Pinshane Y. Huang − *Department of Materials Science and Engineering, University of Illinois Urbana−Champaign, Urbana, Illinois 61801, United States; Materials Research Laboratory, University of Illinois at Urbana−Champaign, Urbana, Illinois 61801, United States;* orcid.org/0000-0002-1095-1833; Email: pyhuang@illinois.edu

Authors

Chia-Hao Lee − *Department of Materials Science and Engineering, University of Illinois Urbana−Champaign, Urbana, Illinois 61801, United States*

Abid Khan − *Department of Physics, University of Illinois Urbana−Champaign, Urbana, Illinois 61801, United States*

Di Luo − *Department of Physics, University of Illinois Urbana−Champaign, Urbana, Illinois 61801, United States*

Tatiane P. Santos − *Department of Materials Science and Engineering, University of Illinois Urbana−Champaign, Urbana, Illinois 61801, United States*

Chuqiao Shi − *Department of Materials Science and Engineering, University of Illinois Urbana−Champaign, Urbana, Illinois 61801, United States*

Blanka E. Janicek – *Department of Materials Science and Engineering, University of Illinois Urbana–Champaign, Urbana, Illinois 61801, United States;* orcid.org/0000-0002-5529-2819

Sangmin Kang – *Department of Electrical and Computer Engineering, University of Illinois Urbana–Champaign, Urbana, Illinois 61801, United States*

Wenjuan Zhu – *Department of Electrical and Computer Engineering, University of Illinois Urbana–Champaign, Urbana, Illinois 61801, United States;* orcid.org/0000-0003-2824-1386

Nahil A. Sobh – *Beckman Institute for Advanced Science and Technology, University of Illinois Urbana–Champaign, Urbana, Illinois 61801, United States*

André Schleife – *Department of Materials Science and Engineering, University of Illinois Urbana–Champaign, Urbana, Illinois 61801, United States; Materials Research Laboratory and National Center for Supercomputing Applications, University of Illinois at Urbana–Champaign, Urbana, Illinois 61801, United States;* orcid.org/0000-0003-0496-8214

Bryan K. Clark – *Department of Physics, University of Illinois Urbana–Champaign, Urbana, Illinois 61801, United States*

Complete contact information is available at:
https://pubs.acs.org/10.1021/acs.nanolett.0c00269

Author Contributions

[#]These authors contributed equally to this work. Under supervision by P.Y.H., C.-H.L. analyzed the preliminary STEM images acquired by B.E.J. and performed $WSe_{2-2x}Te_{2x}$ TEM sample preparation, STEM imaging, data analysis, and elastic theory modeling. Under supervision by P.Y.H., C.-H.L. and C.S. generated simulated STEM images for FCNs training. Under supervision by B.K.C., D.L. and A.K. constructed the FCN models. N.A.S. contributed to the FCN structure and performance evaluation. Under supervision by A.S., T.S. performed DFT calculations. Under supervision by W.Z., S.K. synthesized the 2D $WSe_{2-2x}Te_{2x}$ flakes. All authors read and contributed to the manuscript.

Notes

The authors declare no competing financial interest.

ACKNOWLEDGMENTS

This work was primarily funded by the Air Force Office of Scientific Research under award FA9550-17-1-0213 (STEM experiments) and by the U.S. Department of Energy, Office of Basic Energy Sciences, Division of Materials Sciences and Engineering under award DE-SC0020190 (deep learning and data analysis). Synthesis of the sample was funded by the Office of Naval Research under award NAVY N00014-17-1-2973. Computational work (DFT simulation) was funded by the Office of Naval Research under award NAVY N00014-18-1-2605, by the National Science Foundation under awards OCI-0725070 and ACI-1238993, by the state of Illinois, and also made use of Blue Waters Supercomputer and Illinois Campus Cluster, which are supported by funds from University of Illinois at Urbana–Champaign. This work was carried out in part in Materials Research Laboratory Central Facilities at the University of Illinois at Urbana–Champaign. The authors thank Prof. Paul Voyles, Prof. Elif Ertekin, Dr. Colin Ophus, and Prof. Dallas Trinkle for helpful discussions.

REFERENCES

(1) Feng, J.; Qian, X.; Huang, C. W.; Li, J. Strain-engineered artificial atom as a broad-spectrum solar energy funnel. *Nat. Photonics* **2012**, *6*, 866–872.

(2) Van Der Zande, A. M.; Huang, P. Y.; Chenet, D. A.; Berkelbach, T. C.; You, Y.; Lee, G. H.; Heinz, T. F.; Reichman, D. R.; Muller, D. A.; Hone, J. C. Grains and grain boundaries in highly crystalline monolayer molybdenum disulphide. *Nat. Mater.* **2013**, *12*, 554–561.

(3) Lin, Z.; Carvalho, B. R.; Kahn, E.; Lv, R.; Rao, R.; Terrones, H.; Pimenta, M. A.; Terrones, M. Defect engineering of two-dimensional transition metal dichalcogenides. *2D Mater.* **2016**, *3*, 022002.

(4) Huang, P. Y.; Kurasch, S.; Alden, J. S.; Shekhawat, A.; Alemi, A. A.; McEuen, P. L.; Sethna, J. P.; Kaiser, U.; Muller, D. A. Imaging Atomic Rearrangements in Two-Dimensional Silica Glass: Watching Silica's Dance. *Science* **2013**, *342*, 224–227.

(5) Wang, S.; Lee, G. D.; Lee, S.; Yoon, E.; Warner, J. H. Detailed Atomic Reconstruction of Extended Line Defects in Monolayer MoS2. *ACS Nano* **2016**, *10*, 5419–5430.

(6) Azizi, A.; Wang, Y.; Stone, G.; Elias, A. L.; Lin, Z.; Terrones, M.; Crespi, V. H.; Alem, N. Defect Coupling and Sub-Angstrom Structural Distortions in W1-xMoxS2 Monolayers. *Nano Lett.* **2017**, *17*, 2802–2808.

(7) Van Aert, S.; Den Dekker, A. J.; Van Dyck, D.; Van Den Bos, A. Optimal experimental design of STEM measurement of atom column positions. *Ultramicroscopy* **2002**, *90*, 273–289.

(8) Komsa, H. P.; Kurasch, S.; Lehtinen, O.; Kaiser, U.; Krasheninnikov, A. V. From point to extended defects in two-dimensional MoS2: Evolution of atomic structure under electron irradiation. *Phys. Rev. B: Condens. Matter Mater. Phys.* **2013**, *88*, 035301.

(9) Algara-Siller, G.; Kurasch, S.; Sedighi, M.; Lehtinen, O.; Kaiser, U. The pristine atomic structure of MoS2 monolayer protected from electron radiation damage by graphene. *Appl. Phys. Lett.* **2013**, *103*, 203107.

(10) Elibol, K.; Susi, T.; Argentero, G.; Reza Ahmadpour Monazam, M.; Pennycook, T. J.; Meyer, J. C.; Kotakoski, J. Atomic Structure of Intrinsic and Electron-Irradiation-Induced Defects in MoTe2. *Chem. Mater.* **2018**, *30*, 1230–1238.

(11) Ophus, C.; Ciston, J.; Nelson, C. T. Correcting nonlinear drift distortion of scanning probe and scanning transmission electron microscopies from image pairs with orthogonal scan directions. *Ultramicroscopy* **2016**, *162*, 1–9.

(12) Zuo, J. M.; Shah, A. B.; Kim, H.; Meng, Y.; Gao, W.; Rouviére, J. L. Lattice and strain analysis of atomic resolution Z-contrast images based on template matching. *Ultramicroscopy* **2014**, *136*, 50–60.

(13) Mevenkamp, N.; Binev, P.; Dahmen, W.; Voyles, P. M.; Yankovich, A. B.; Berkels, B. Poisson noise removal from high-resolution STEM images based on periodic block matching. *Adv. Struct. Chem. Imag.* **2015**, *1*, 3.

(14) Kimoto, K.; Asaka, T.; Yu, X.; Nagai, T.; Matsui, Y.; Ishizuka, K. Local crystal structure analysis with several picometer precision using scanning transmission electron microscopy. *Ultramicroscopy* **2010**, *110*, 778–782.

(15) Yankovich, A. B.; Berkels, B.; Dahmen, W.; Binev, P.; Sanchez, S. I.; Bradley, S. A.; Li, A.; Szlufarska, I.; Voyles, P. M. Picometre-precision analysis of scanning transmission electron microscopy images of platinum nanocatalysts. *Nat. Commun.* **2014**, *5*, 4155.

(16) Han, Y.; Nguyen, K.; Cao, M.; Cueva, P.; Xie, S.; Tate, M. W.; Purohit, P.; Gruner, S. M.; Park, J.; Muller, D. A. Strain Mapping of Two-Dimensional Heterostructures with subpicometer Precision. *Nano Lett.* **2018**, *18*, 3746–3751.

(17) Warner, J. H.; Margine, E. R.; Mukai, M.; Robertson, A. W.; Giustino, F.; Kirkland, A. I. Dislocation-driven deformations in graphene. *Science* **2012**, *337*, 209–212.

(18) Robertson, A. W.; Montanari, B.; He, K.; Allen, C. S.; Wu, Y. A.; Harrison, N. M.; Kirkland, A. I.; Warner, J. H. Structural reconstruction of the graphene monovacancy. *ACS Nano* **2013**, *7*, 4495–4502.

(19) Chen, Q.; Robertson, A. W.; He, K.; Gong, C.; Yoon, E.; Lee, G. D.; Warner, J. H. Atomic Level Distributed Strain within Graphene Divacancies from Bond Rotations. *ACS Nano* **2015**, *9*, 8599−8608.
(20) Cheng, Y.; Walz, T. The Advent of Near-Atomic Resolution in Single-Particle Electron Microscopy. *Annu. Rev. Biochem.* **2009**, *78*, 723−742.
(21) Tizei, L. H.; Lin, Y. C.; Mukai, M.; Sawada, H.; Lu, A. Y.; Li, L. J.; Kimoto, K.; Suenaga, K. Exciton Mapping at Subwavelength Scales in Two-Dimensional Materials. *Phys. Rev. Lett.* **2015**, *114*, 107601.
(22) Rhodes, D.; et al. Engineering the Structural and Electronic Phases of MoTe2 through W Substitution. *Nano Lett.* **2017**, *17*, 1616−1622.
(23) Apte, A.; Krishnamoorthy, A.; Hachtel, J. A.; Susarla, S.; Idrobo, J. C.; Nakano, A.; Kalia, R. K.; Vashishta, P.; Tiwary, C. S.; Ajayan, P. M. Telluride-Based Atomically Thin Layers of Ternary Two-Dimensional Transition Metal Dichalcogenide Alloys. *Chem. Mater.* **2018**, *30*, 7262−7268.
(24) Lin, J.; Zhou, J.; Zuluaga, S.; Yu, P.; Gu, M.; Liu, Z.; Pantelides, S. T.; Suenaga, K. Anisotropic Ordering in 1T' Molybdenum and Tungsten Ditelluride Layers Alloyed with Sulfur and Selenium. *ACS Nano* **2018**, *12*, 894−901.
(25) Savitzky, B. H.; et al. Image registration of low signal-to-noise cryo-STEM data. *Ultramicroscopy* **2018**, *191*, 56−65.
(26) Ziatdinov, M.; Dyck, O.; Maksov, A.; Li, X.; Sang, X.; Xiao, K.; Unocic, R. R.; Vasudevan, R.; Jesse, S.; Kalinin, S. V. Deep Learning of Atomically Resolved Scanning Transmission Electron Microscopy Images: Chemical Identification and Tracking Local Transformations. *ACS Nano* **2017**, *11*, 12742−12752.
(27) Madsen, J.; Liu, P.; Kling, J.; Wagner, J. B.; Hansen, T. W.; Winther, O.; Schiøtz, J. A deep learning approach to identify local structures in atomic-resolution transmission electron microscopy images. *Advanced Theory and Simulation* **2018**, *1*, 1800037.
(28) Maksov, A.; Dyck, O.; Wang, K.; Xiao, K.; Geohegan, D. B.; Sumpter, B. G.; Vasudevan, R. K.; Jesse, S.; Kalinin, S. V.; Ziatdinov, M. Deep learning analysis of defect and phase evolution during electron beam-induced transformations in WS2. *npj Comput. Mater.* **2019**, *5*, 12.
(29) Lin, W.; Li, Q.; Belianinov, A.; Sales, B. C.; Sefat, A.; Gai, Z.; Baddorf, A. P.; Pan, M.; Jesse, S.; Kalinin, S. V. Local crystallography analysis for atomically resolved scanning tunneling microscopy images. *Nanotechnology* **2013**, *24*, 415707.
(30) Gong, Y.; et al. Band gap engineering and layer-by-layer mapping of selenium-doped molybdenum disulfide. *Nano Lett.* **2014**, *14*, 442−449.
(31) Kirkland, E. J. *Computem*. http://sourceforge.net/projects/computem (accessed 2018/09/16).
(32) Kirkland, E. J. *Advanced Computing in Electron Microscopy*; Springer: New York, 2010.
(33) Efron, B. Bootstrap methods: Another look at jackknife. *Annals of Statistics* **1979**, *7*, 1−26.
(34) Eshelby, J. D. The determination of the elastic field of an ellipsoidal inclusion, and related problems. *Proc. R. Soc. London, Ser. A* **1957**, *241*, 376−396.
(35) Mura, T. *Micromechanics of defects in solids*; Martinus Nijhoff Publishers: The Hague, 1982.
(36) Kolesnikova, A. L.; Orlova, T. S.; Hussainova, I.; Romanov, A. E. Elastic models of defects in two-dimensional crystals. *Phys. Solid State* **2014**, *56*, 2573−2579.
(37) Kanzaki, H. Point Defects in Face-Centred Distortion Cubic Lattice-Distortion around Defects. *J. Phys. Chem. Solids* **1957**, *2*, 24−36.
(38) Hall, G. L. Distortion Around Simple Point Imperfections in Simple Crystals. *J. Phys. Chem. Solids* **1957**, *3*, 210−222.
(39) Råsander, M.; Moram, M. A. On the accuracy of commonly used density functional approximations in determining the elastic constants of insulators and semiconductors. *J. Chem. Phys.* **2015**, *143*, 144104.
(40) Girifalco, L. A.; Weizer, V. G. Vacancy relaxation in cubic crystals. *J. Phys. Chem. Solids* **1960**, *12*, 260−264.
(41) Hardy, J. R. A theoretical study of point defects in the rocksalt structure substitutional K+ in NaCl. *J. Phys. Chem. Solids* **1960**, *15*, 39−49.
(42) Singhal, S. P. Lattice Relaxations near a Vacancy or Interstitial in Al. *Phys. Rev. B* **1973**, *8*, 3641−3949.
(43) Tewary, V. K. Green-function method for lattice statics. *Adv. Phys.* **1973**, *22*, 757−810.
(44) Trinkle, D. R. Lattice Green function for extended defect calculations: Computation and error estimation with long-range forces. *Phys. Rev. B: Condens. Matter Mater. Phys.* **2008**, *78*, 014110.